

## Article

# Electromagnetic Torque Analysis and Structure Optimization of Interior Permanent Magnet Synchronous Machine with Air-Gap Eccentricity

Jing Wang and Yubin Wang \* 

College of New Energy, China University of Petroleum (East China), Qingdao 266580, China

\* Correspondence: wangyubin@upc.edu.cn; Tel.: +86-155-8867-0358

**Abstract:** Interior permanent magnet synchronous machine with air-gap eccentricity (AGE-IPMSM) has the advantages of low torque ripple and low noise. However, air-gap eccentricity will lower the power density of the machine to a certain extent. In this paper, an 18-slot/8-pole interior permanent magnet synchronous machine with air-gap eccentricity is taken as the research object. According to the magnetic circuit method, the no-load and load air-gap magnetic field analytical models are calculated, respectively. Then, by Maxwell's tensor method, the variation law of radial and tangential air-gap magnetic density harmonic amplitudes and phase angle difference cosine values are analyzed, and it is concluded that the electromagnetic torque can be improved by increasing phase angle difference cosine values of the magnetic density harmonic, which produces the driving torque after eccentricity. On this basis, in order to improve the output characteristics of the machine, the eccentricity and the angle between the V-type permanent magnets are optimized with the total harmonic distortion (THD), electromagnetic torque, and torque ripple as the optimization goals, and then the optimal structure size parameters of the machine are finally determined. Finally, a prototype is manufactured on the basis of the optimal parameters, and the experimental results of the prototype verify the validity and correctness of the theoretical analysis and finite element analysis (FEA).

**Keywords:** IPM synchronous machine; air-gap eccentricity; Maxwell's tensor method; analysis of torque harmonic



**Citation:** Wang, J.; Wang, Y.

Electromagnetic Torque Analysis and Structure Optimization of Interior Permanent Magnet Synchronous Machine with Air-Gap Eccentricity. *Energies* **2023**, *16*, 1665. <https://doi.org/10.3390/en16041665>

Academic Editor: Andrea Mariscotti

Received: 17 January 2023

Revised: 3 February 2023

Accepted: 4 February 2023

Published: 7 February 2023



**Copyright:** © 2023 by the authors. Licensee MDPI, Basel, Switzerland. This article is an open access article distributed under the terms and conditions of the Creative Commons Attribution (CC BY) license (<https://creativecommons.org/licenses/by/4.0/>).

## 1. Introduction

With the increasing cost performance of rare earth permanent magnetic materials, permanent magnet machines have been applied far and wide in electric vehicles, new energy power generation, and aviation power actuation systems by virtue of their excellent control performance, high power density, and high efficiency [1–4]. According to the different positions of permanent magnets in the rotor, permanent magnet synchronous machines can usually be divided into two categories: surface-mounted permanent-magnet synchronous machines (SPMSMs) [5,6] and interior permanent-magnet synchronous machines (IPMSMs) [7]. Compared with SPMSMs, the magnetic path of IPMSMs is asymmetric, and its d-axis and q-axis inductances are different, which can produce reluctance torque, so it has high overload capacity and torque density and has a wide range of constant power operation, which can easily realize flux-weakening speed adjusting. Therefore, interior permanent-magnet synchronous machines are widely used in the field of electric vehicle driving machines [8–10].

However, while having the above advantages, IPMSMs also have disadvantages, such as large torque ripple, electromagnetic vibration, and noise [3]. The torque ripple and electromagnetic vibration of the machine will lead to bearing wear and the decrease of winding insulation capability, thus affecting the service life of the machine [11,12]. Therefore, in order to reduce the torque ripple of IPMSMs, domestic and foreign scholars have carried out many studies on this. Assuming that the stator winding current of the

machine is an ideal sinusoidal wave, the influence of iron core saturation is ignored, and the torque fluctuation of IPMSMs comes mainly from cogging torque and electromagnetic torque. A SPMSM with partially segmented Halbach structure is designed, whereby its permanent magnet is magnetized by Halbach magnetization method [13]. Each pole is divided into three portions, one side of the main magnetic pole is partially segmented, and the thickness and width of the boundary pole and the main pole are unequal. Although the structure can reduce the cogging torque, it is more suitable for SPMSMs. In addition, the rotor skew pole can also reduce the cogging torque, but this method will reduce the back electromotive force (EMF) and average torque to a certain extent, and the machining process of the skew pole is difficult [14]. Tooth harmonics and phase band harmonics in the back EMF are the main cause of electromagnetic torque pulsation. Multilayer windings can suppress even harmonics in the back EMF and, thus, reduce torque ripple, but this method is limited to special pole–slot combinations [15]. For the sake of reducing both the cogging torque and the electromagnetic torque fluctuation, it can be lowered by changing the rotor shape in the reference [16,17], including the pole arc eccentric cutting pole, sine cutting pole, inverse cosine cutting pole, etc. However, there is a contradiction between torque ripple suppression and electromagnetic torque loss in the above methods.

Accordingly, how to reduce torque ripple while increasing the power density is an urgent problem for PMSMs. A new type of PMSM based on the armature reaction compensation principle was proposed in the reference [18], that is, a set of current-controlled q-axis excitation windings is added to the rotor of PMSM to compensate for the armature reaction magnetomotive force (MMF) to ensure that the air-gap magnetic field remains basically constant when the load changes, breaking the limit of magnetic saturation on the electromagnetic torque and improving the torque density, but this method does not consider the effect on the torque ripple. A new hybrid rotor permanent magnet (HRPM) machine was proposed in the reference [19], capable of combining high PM torque of surface-inserted PMSM with high reluctance torque of IPMSM, and the average torque is improved and the torque fluctuation is reduced by introducing shifting angle of SPMSMs and open angle of air barriers, respectively. The output torque was enhanced by injecting third-harmonic back-EMF and armature current in dual three-phase permanent magnet machines [20]. The optimal third harmonic injection method was utilized to improve the torque density by changing the shape of the permanent magnets for five-phase SPMSMs in the reference [21,22], while the rotor shape of the inverse cosine IPMSM was improved to increase the average torque, and the torque ripple remains almost constant. Although the above method can increase the output torque, it is not applicable to all AGE-IPMSMs.

To address the above-mentioned issues, an 18-slot/8-pole AGE-IPMSM is taken as the research object in this paper. First, according to the magnetic circuit method, the no-load and load air-gap magnetic field analytical models are calculated, respectively. Then, by Maxwell's tensor method, the variation law of radial and tangential air-gap magnetic density harmonic amplitudes and phase angle cosine values are analyzed, and the mechanism of air-gap eccentricity affecting electromagnetic torque is revealed. On the basis of this theory, the output characteristics of the machine is improved. The eccentricity and the angle between the V-type permanent magnets are optimized with the total harmonic distortion, electromagnetic torque, and torque ripple as the optimization goals, and then the optimal structure size parameters of the machine are finally determined. Finally, the validity and correctness of the theoretical analysis and finite element simulation are verified through prototype experiments.

## 2. AGE-IPMSM Structure and Air-Gap Magnetic Field Analysis

### 2.1. Analysis of Air-Gap Eccentric Structure and Air-Gap Permeance

For the conventional IPMSM with uniform air gap, the air-gap magnetic field waveform does not follow a sinusoidal distribution but rather a trapezoidal distribution owing to the characteristics of the magnetic circuit of IPMSM. In the machine design, it is necessary to keep the air-gap field waveform as sinusoidal as possible, which can effectively reduce

the torque ripple. By optimizing the uniform air gap into a non-uniform air gap, the air-gap flux density waveform can be adjusted to eliminate or suppress part of harmonics and improve the output characteristics of the machine. The topological structure of AGE-IPMSM is shown in Figure 1a, and the air-gap eccentric structure is shown in Figure 1b. For the uniform air-gap structure, the air-gap length  $\delta_0$  is a constant value, while the air-gap length is a function of the central angle  $\theta$  for the non-uniform air-gap structure,  $h$  is the eccentricity distance,  $\theta_r$  is half of the central angle of each pole air gap,  $R_r$  is the rotor radius with uniform air gap, and  $\delta_r(\theta)$  is the equivalent air-gap length after air-gap eccentricity.

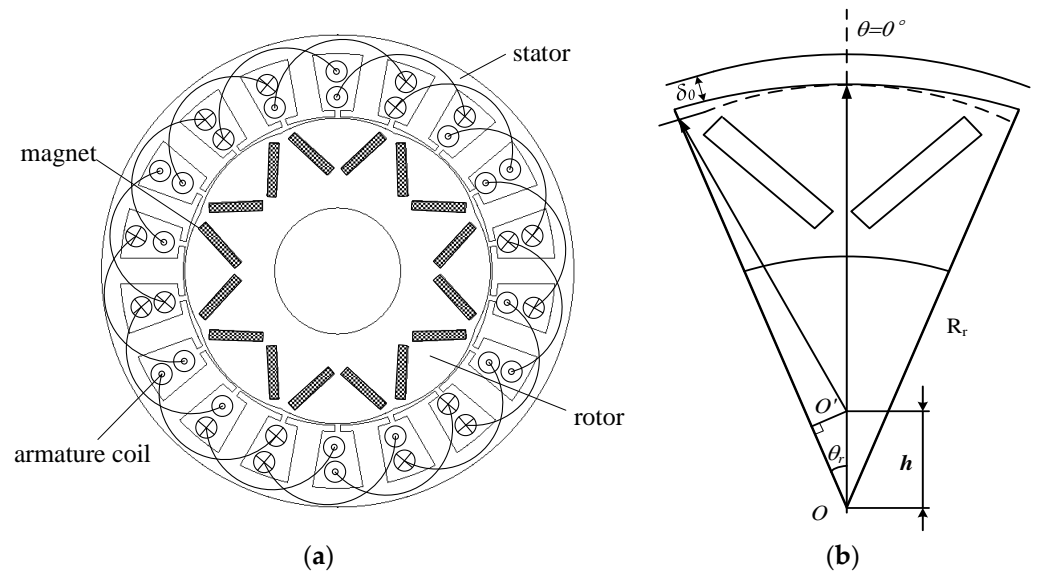


**Figure 1.** (a) Topological structure of AGE-IPMSM. (b) Schematic diagram of air-gap eccentric structure.

From the air-gap eccentric structure shown in Figure 1b, it can be geometrically deduced that the air-gap length is

$$\delta_r(\theta) = R_r - \left[ h \cos \theta + \sqrt{(R_r - h)^2 - (h \sin \theta)^2} \right] \quad (1)$$

On the basis of Equation (1), the air-gap length decreases with the decrease of the circular center angle. Because of the uneven distribution of air-gap permeability in the eccentric air gap, the air-gap permeability at the q-axis is smaller than that at the center of the d-axis magnetic pole, and flux lines are more concentrated at the center of the d-axis pole compared with the non-eccentric case, so the magnetic density  $B_{max}$  at the center of the d-axis pole after eccentricity is larger than that of  $B_\delta$  at the non-eccentric time, and the eccentricity coefficient is introduced to characterize the effect of air-gap eccentricity on the magnetic field. Keeping the magnetic flux per pole constant before and after eccentricity, the following equation is obtained.

$$\int_{-\theta_r}^{\theta_r} B_{max} \frac{\delta}{\delta + \delta_r(\theta)} d\theta = B_\delta 2\theta_r \quad (2)$$

The eccentricity coefficient is determined from  $B_{max}$ , and, thus, the air-gap permeability function of the air-gap eccentricity can be expressed as:

$$\Lambda_r(\theta) = \frac{k_c \mu_0}{\delta_0 + \delta_r(\theta)} \quad (3)$$

where  $\mu_0$  is the air permeability, and  $\delta_0$  is the original length of air gap. The air-gap permeability waveform under air-gap eccentricity in one circle is obtained according to Equation (3), as shown in Figure 2, which is approximated as a sinusoidal waveform. The

Fourier transform of this waveform, with the change of circumferential position of the air-gap permeance can be derived as:

$$\Lambda_r(\theta) = \Lambda_{r0} + \sum_{j=1}^{\infty} \Lambda_j \cos(2jp\theta) \tag{4}$$

where  $\Lambda_{r0}$  is the DC component of the air-gap permeance,  $\Lambda_j$  is the  $j$ th harmonic component of the air-gap permeability ( $j = 1, 2, 3 \dots$ ), and  $p$  is the number of pole pairs.

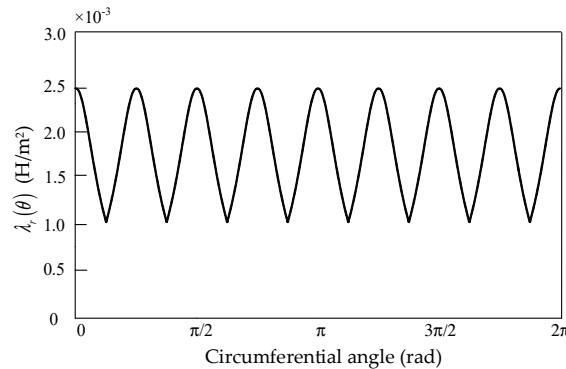


Figure 2. Air-gap permeance waveform of air-gap eccentricity.

The stator core slotting will change the equivalent air-gap length, and the value of the air-gap permeance function is also affected. Accordingly, the influence of the stator cogging effect on the air-gap magnetic field needs to be considered when calculating the air-gap permeance function. Under ideal conditions, flux lines will fully penetrate into the stator core to form a closed loop. In fact, as a result of the stator slotting, the lengths of a small quantity of flux lines that penetrate into the stator slot are much smaller than the deepness of the stator slot, so only the length of the flux line of the slot opening part can be calculated.

According to the principle of minimum magnetoresistance, flux lines always form a closed circuit along the path of minimum magnetic reluctance. The schematic diagram of magnetic flux lines path in stator slot is shown in Figure 3. The flux lines in stator slots will penetrate into the slot perpendicularly and split into two parts,  $l_1$  and  $l_2$ , since the magnetic permeability of the iron core is much greater than the air magnetic permeability, and then it will penetrate into the stator teeth on both sides along the direction of 1/4 circle, respectively. After the parallel connection of the two paths, the length of the flux lines is the equivalent air-gap length of the stator slot opening, which is expressed as:

$$\delta_s(\theta) = \begin{cases} \pi R_s \frac{\sin(\frac{\theta_s}{4} + \frac{\theta}{2}) \sin(\frac{\theta_s}{4} - \frac{\theta}{2})}{\sin(\frac{\theta_s}{4} + \frac{\theta}{2}) + \sin(\frac{\theta_s}{4} - \frac{\theta}{2})}, & \theta \in (-\frac{\theta_s}{2}, \frac{\theta_s}{2}) \\ 0, & \theta \in (\frac{\theta_s}{2}, \frac{\theta_s + \theta_t}{2}) \cup (-\frac{\theta_s + \theta_t}{2}, -\frac{\theta_s}{2}) \end{cases} \tag{5}$$

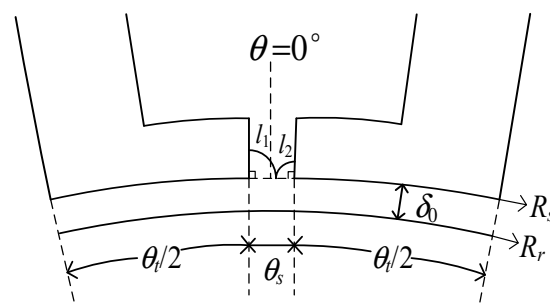


Figure 3. Schematic diagram of magnetic flux lines path in stator slot.

The air-gap permeability function of the stator cogging effect can be derived as:

$$\Lambda_s(\theta) = \frac{\mu_0}{\delta_0 + \delta_s(\theta)} \tag{6}$$

The air-gap permeability waveform of the stator cogging effect in one circle is obtained according to Equation (6), as shown in Figure 4. The Fourier transform of this waveform, with the change of circumferential position of the air-gap permeability can be calculated as:

$$\Lambda_s(\theta) = \Lambda_{s0} + \sum_{k=1}^{\infty} \Lambda_k \cos(kZ\theta) \tag{7}$$

where  $\Lambda_{s0}$  is the DC component of the air-gap permeability,  $\Lambda_k$  is the  $k$ th harmonic component of the air-gap permeability ( $k = 1, 2, 3 \dots$ ), and  $Z$  is the number of pole pairs.

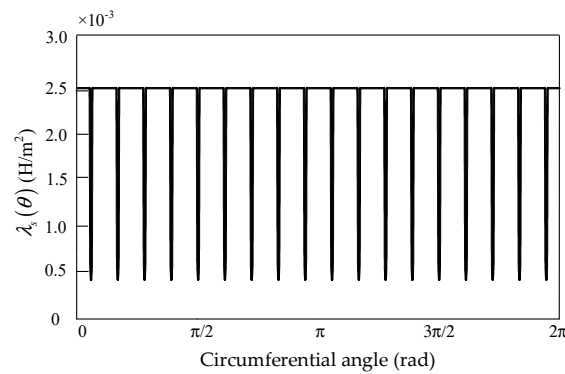


Figure 4. Air-gap permeance waveform of stator slotting.

### 2.2. Analysis of No-Load Air-Gap Magnetic Field

Under the no-load condition, the permanent magnet field interacts with the stator slot and eccentricity to generate the air-gap magnetic field, of which each pole can be approximated as trapezoidal wave if the stator slotting and eccentricity are ignored. The permanent magnet magnetic field distribution and MMF waveform of AGE-IPMSM are shown in Figure 5.

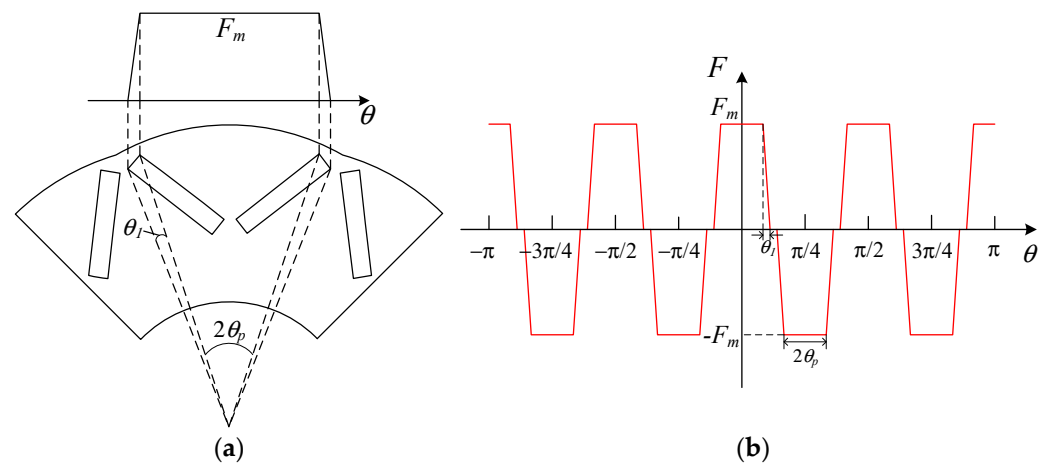


Figure 5. Permanent magnet magnetomotive force of AGE-IPMSM: (a) permanent magnetic field distribution and (b) permanent magnet MMF.

By performing a Fourier decomposition on the waveform shown in Figure 5, the per-pole air-gap MMF is expressed as:

$$\begin{cases} f_{mr}(\theta, t) = \sum_{n=1,3,5}^{\infty} F_{mn} \cos(np\theta - n\omega t) \\ F_{mn} = \frac{8F_m}{n^2\pi p\theta_1} \sin \frac{np(2\theta_p + \theta_1)}{2} \sin \frac{np\theta_1}{2} \end{cases} \quad (8)$$

where  $\theta_p$  and  $\theta_1$  are the permanent magnet angle parameters,  $p = 4$  is the number of pole pairs,  $n = 1,3,5 \dots$ ,  $F_{mn}$  is the  $n$ th component amplitude, and  $F_m$  is the MMF provided by each pole of PM to the external magnetic circuit, of which the total flux can be split into two portions, one portion with the linkage of armature windings, called the main flux, and the other portion without the linkage, called the leakage flux. The schematic diagram of magnetic force lines path is shown in Figure 6a. The equivalent magnetic circuit model of AGE-IPMSM can be obtained according to the equivalent magnetic circuit method, as shown in Figure 6b, where  $F_c$  is the constant MMF per pole of permanent magnet,  $R_m$  is the permanent magnet reluctance,  $\Phi_m$  is the total magnetic flux supplied by each pole of PM to the external magnetic circuit,  $R_\sigma$  is the permanent magnet's own leakage reluctance,  $R'_\sigma$  is the permanent magnet inter-pole leakage reluctance,  $\Phi_\sigma$  is the permanent magnet's own leakage flux,  $\Phi'_\sigma$  is the inter-pole leakage flux of the PM,  $R_\delta$  is the equivalent air-gap reluctance, and  $\Phi_\delta$  is the main flux (i.e., air-gap flux per pole).

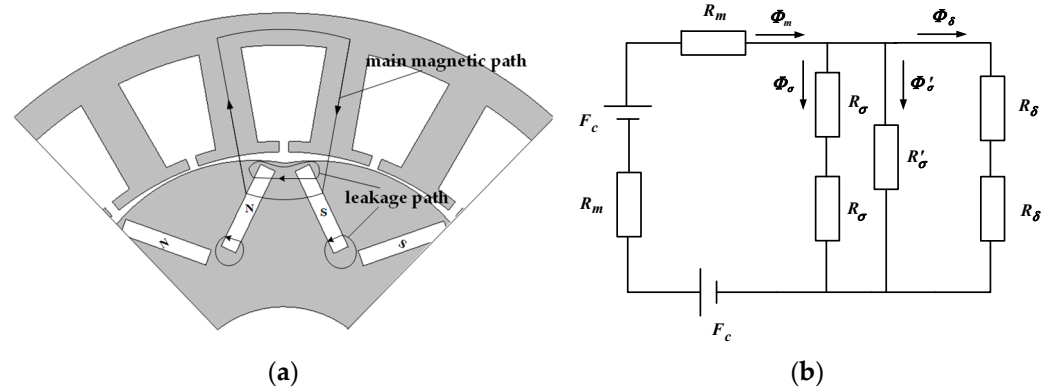


Figure 6. (a) Schematic diagram of magnetic flux lines path. (b) Equivalent magnetic circuit model.

In accordance with the equivalent magnetic circuit model, the magnetic flux and the MMF supplied to the external circuit by each pole of the permanent magnet can be calculated as:

$$\begin{cases} \Phi_m = \Phi_\delta + \Phi_\sigma = \frac{F_c}{R_m + \frac{R_\sigma R'_\sigma R_\delta}{R_\delta(2R_\sigma + R'_\sigma) + R_\sigma R'_\sigma}} \\ F_m = \Phi_m R_\delta = \frac{F_c}{\frac{R_m}{R_\delta} + \frac{R_\sigma R'_\sigma}{R_\sigma R'_\sigma + R_\delta(2R_\sigma + R'_\sigma)}} \end{cases} \quad (9)$$

Combining Equations (4), (7) and (8), the no-load air gap magnetic density can be calculated as:

$$\begin{aligned} B_{mr}(\theta, t) &= \Lambda_s(\theta)\Lambda_r(\theta)f_c(\theta, t) \\ &= \sum_{n=1,3,5}^{+\infty} \Lambda_{s0}\Lambda_{r0}F_{mn} \cos(np\theta - n\omega t) \\ &+ \frac{1}{2} \sum_{n=1,3,5}^{+\infty} \sum_{k=1}^{+\infty} \Lambda_{r0}\Lambda_k F_{mn} \cos[(np \pm kZ)\theta - n\omega t] \\ &+ \frac{1}{2} \sum_{n=1,3,5}^{+\infty} \sum_{j=1}^{+\infty} \Lambda_{s0}\Lambda_j F_{mn} \cos[(2jp \pm np)\theta - (2j \pm n)\omega t] \\ &+ \frac{1}{4} \sum_{n=1,3,5}^{+\infty} \sum_{k=1}^{+\infty} \sum_{j=1}^{+\infty} \Lambda_j\Lambda_k F_{mn} \cos[(2jp \pm kZ \pm np)\theta - (2j \pm n)\omega t] \end{aligned} \quad (10)$$

According to Equation (10), the analytic waveform of air-gap magnetic density after air-gap eccentricity can be obtained. The comparison results between the analytic calculation and the FEA waveform are shown in Figure 7, from which it can be seen that analytical results are basically consistent with the FEA, thus verifying the accuracy of the analytic calculation.

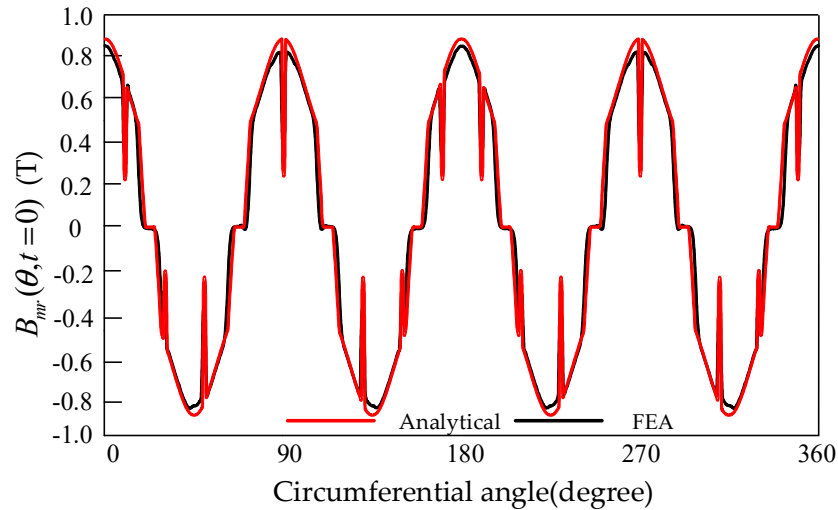


Figure 7. Comparison between analytical results and FEA of no-load air-gap flux density.

### 2.3. Analysis of Load Air-Gap Magnetic Field

The air-gap magnetic field under load is formed by the interaction of the no-load air-gap magnetic field and the armature reaction magnetic field. The following assumptions must be made when calculating the armature reaction magnetic field of AGE-IPMSM:

1. Ignoring the core saturation of stator and rotor;
2. Ignoring the influence of end winding on armature reaction magnetic field.

The number of turns of the fractional slot distribution winding is  $N_c$ , the winding pitch is  $y = 2$ , the sinusoidal AC current  $i(t) = \sqrt{2}I \cos \omega t$ , with the frequency  $\omega$ , the RMS value  $I$  is input, and the total MMF is  $iN_c$ . The origin of the space coordinate is taken on the axial line of the A-phase winding. When the symmetrical three-phase windings are supplied with the symmetrical three-phase AC current with a time difference of  $2\pi/3$ , the synthetic MMF of the A, B, C three-phase windings can be expressed as:

$$\begin{cases} f_{ar}(\theta, t) = f_A(\theta, t) + f_B(\theta, t) + f_C(\theta, t) \\ = \sum_{v=2,8,14,\dots,6n+2}^{+\infty} 3F_{mv} (2 \cos \frac{2\pi}{9}v - 1) \cos(v\theta + \omega t + \varphi_0) \\ + \sum_{v=4,10,16,\dots,6n-2}^{+\infty} 3F_{mv} (2 \cos \frac{2\pi}{9}v - 1) \cos(v\theta - \omega t - \varphi_0) \\ F_{mv} = \frac{2\sqrt{2}N_c I}{v\pi} \sin \frac{v\pi}{9} \end{cases} \quad (11)$$

where  $F_{mv}$  is the MMF amplitude of one coil,  $\varphi_0$  is the initial phase angle of the three-phase current,  $\omega$  is the three-phase current angular velocity,  $v$  is the number of harmonics, and  $v = 2, 4, 6 \dots$ ,  $\theta$  is the space mechanical angle.

Combining Equations (4), (7) and (11), the air-gap magnetic density of armature reaction magnetic field can be calculated as:

$$\begin{aligned}
 B_{ar}(\theta, t) &= f_{ar}(\theta, t)\Lambda_s(\theta)\Lambda_r(\theta) \\
 &= \sum_{v=2,4,6}^{+\infty} \Lambda_{s0}\Lambda_{r0}F_{amv} \cos[v\theta - h(\omega t + \varphi_0)] \\
 &+ \frac{1}{2} \sum_{v=2,4,6}^{+\infty} \sum_{j=1}^{+\infty} \Lambda_{s0}\Lambda_j F_{amv} \cos[(v \pm 2jp)\theta - h(\omega t + \varphi_0)] \\
 &+ \frac{1}{2} \sum_{v=2,4,6}^{+\infty} \sum_{k=1}^{+\infty} \Lambda_{r0}\Lambda_k F_{amv} \cos[(v \pm kZ)\theta - h(\omega t + \varphi_0)] \\
 &+ \frac{1}{4} \sum_{v=2,4,6}^{+\infty} \sum_{k=1}^{+\infty} \sum_{j=1}^{+\infty} \Lambda_k\Lambda_j F_{amv} \cos[(v + kZ \pm 2jp)\theta - h(\omega t + \varphi_0)] \\
 &+ \frac{1}{4} \sum_{v=2,4,6}^{+\infty} \sum_{k=1}^{+\infty} \sum_{j=1}^{+\infty} \Lambda_k\Lambda_j F_{amv} \cos[(v - kZ \mp 2jp)\theta - h(\omega t + \varphi_0)] \\
 F_{amv} &= 3F_{mv}(2 \cos \frac{2\pi}{9}v - 1) = \frac{6\sqrt{2}N_c I}{v\pi}(2 \cos \frac{2\pi}{9}v - 1) \sin \frac{\pi}{9}v
 \end{aligned} \tag{12}$$

where  $F_{amv}$  is the amplitude of the armature reaction MMF,  $h = \begin{cases} 1, v = 6n - 2 \\ -1, v = 6n + 2 \end{cases}$ , and  $n$  is an integer. Under the premise of the stator cogging effect and air-gap eccentricity, the load air-gap magnetic density can be expressed as:

$$B_r = B_{mr} + B_{ar} \tag{13}$$

where  $B_{mr}$  is the no-load air-gap magnetic density, and  $B_{ar}$  is the armature reaction field air-gap magnetic density. In accordance with Equation (13), the analytical waveform of air-gap magnetic density under rated load after air-gap eccentricity can be obtained. The comparison results between the analytic calculation and the FEA waveform are shown in Figure 8, from which it can be seen that there is a certain error between the analytical calculation and the FEA value due to the influence of stator tooth tip saturation, but the change pattern is consistent, which verifies the accuracy of the analytic calculation.

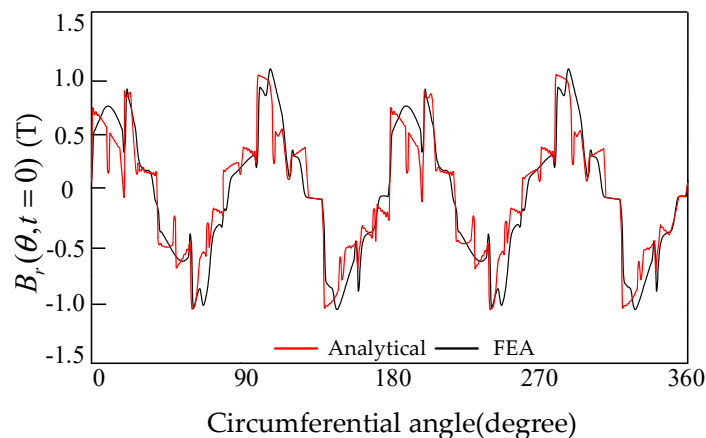


Figure 8. Comparison between analytical results and FEA of rated load air-gap flux density.

#### 2.4. Torque Harmonic Analysis of AGE-IPMSM

The tangential force is generated by the interaction between the harmonics of the no-load permanent magnet magnetic field and the armature reaction magnetic field, which result in electromagnetic torque on the rotor. The Maxwell’s tensor method [23] can be used

to calculate the torque generated by the interaction of each order magnetic flux density on the rotor, as shown in the following:

$$T(t) = \frac{r^2 L_a}{\mu_0} \int_0^{2\pi} B_r(\theta, t) B_t(\theta, t) d\theta = \sum_n T_n(t) \tag{14}$$

$$T_n(t) = \frac{\pi r^2 L_a}{\mu_0} B_{rn} B_{tn} \cos[\theta_{rn}(t) - \theta_{tn}(t)] \tag{15}$$

where  $r$  is the flux density radius,  $L_a$  is the axial length of AGE-IPMSM,  $B_r(\theta, t)$  and  $B_t(\theta, t)$  are the radial flux density and tangential flux density in the air gap, respectively,  $B_{rn}$  and  $B_{tn}$  are the  $n$ th-order radial and tangential flux density harmonic amplitudes, respectively, and  $\theta_{rn}(t)$  and  $\theta_{tn}(t)$  are the corresponding phase angles of the  $n$ th-order radial and tangential flux density harmonic, respectively.

As shown in Figure 9b, most of the amplitude of the radial air-gap magnetic density decreases after eccentricity; only the 20th, 22nd, and 38th harmonics increase, of which the 4th harmonic is fundamental, and the amplitude decreases by 0.08 T after eccentricity, while most of the tangential air-gap magnetic density increases in amplitude after eccentricity, as shown in Figure 9b. Since the tangential air-gap magnetic density is very low, only the fundamental amplitude is selected for comparison, and the amplitude of the fundamental component increases by 0.003 T after eccentricity.

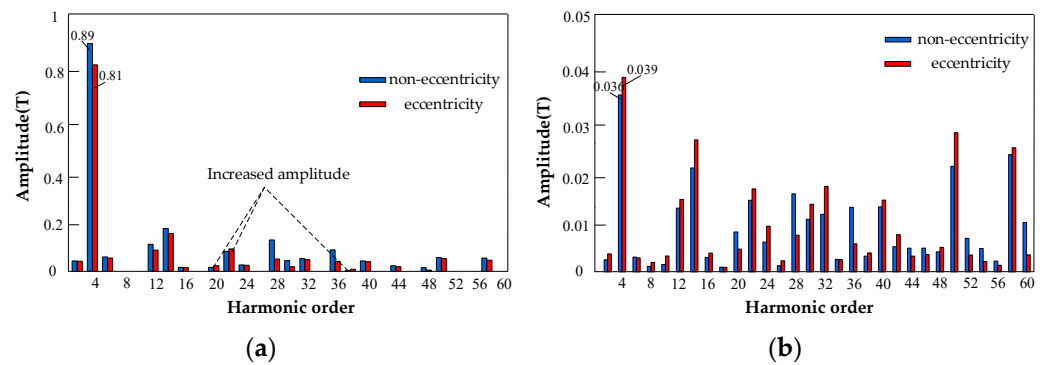


**Figure 9.** Harmonic distribution of radial and tangential air-gap magnetic density: (a) the amplitude of the radial air-gap magnetic density; (b) the amplitude of the tangential air-gap magnetic density.

Through the data in Figure 9, the product of the radial and tangential magnetic density amplitude corresponding to the fundamental component in both cases can be calculated; as shown in Table 1, the amplitude product after eccentricity is only decreased by 0.0004 T, and the change is very little. Therefore, the variation of magnetic density amplitude after air-gap eccentricity has little effect on electromagnetic torque.

**Table 1.** The fundamental component amplitude of the radial and tangential magnetic density in both cases.

	The Amplitude of the Radial Flux Density (T)	The Amplitude of the Tangential Flux Density (T)	Product
Non-eccentricity	0.89	0.036	0.032
Eccentricity	0.81	0.039	0.0316

It can be discovered from Figure 10a that the cosine value of the phase angle difference corresponding to the fundamental component is larger than that of the radial air-gap flux density, and the cosine value of the phase angle difference after the eccentricity is increased by 0.05, which is nearly 100 times larger than the product of the flux density amplitude. Accordingly, it can be explained that the cosine value of the radial and tangential phase

angle difference after air-gap eccentricity has an important influence on electromagnetic torque. The cosine of the phase angle difference for each harmonic is shown in Figure 10b, and it is also found that the cosine increases for most of the harmonics after eccentricity, and only the cosine of the 12th and 36th harmonics decreases.

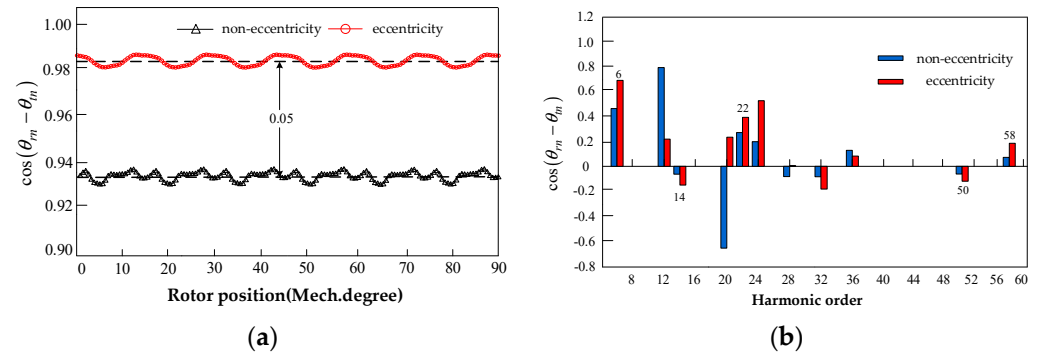


**Figure 10.** Phase angle difference cosine values of radial and tangential magnetic density harmonic: (a) the phase angle difference cosine value of the fundamental component and (b) the cosine value of the phase angle difference for each harmonic.

The torque generated by the fundamental component on the rotor by Maxwell's tensor method is shown in Figure 11a, and the torque generated by the remaining harmonics is shown in Figure 11b. It can be determined from Figure 11a that the electromagnetic torque is formed mainly by the fundamental component, the torque increases by 1.268 Nm after eccentricity, and the torque pulsation is reduced from 5.74% to 2.86%. From the dotted circle in Figure 11b, it can be found that the 20th and 28th harmonics after air-gap eccentricity are transformed from braking torque to driving torque. Comparing Figure 10b with Figure 11b, it can be discovered that the variation law of electromagnetic torque generated by each harmonic is basically consistent with that of the phase angle difference cosine value of each harmonic. After air-gap eccentricity, the driving torque generated by the 6th, 22nd, 24th, and 58th harmonic components increase, while that generated by the 12th and 36th decrease. The braking torque generated by the 14th, 32nd, and 50th harmonic components increase after eccentricity, but the total torque is formed mainly by the fundamental component. Consequently, the air-gap eccentricity can increase the radial and tangential harmonic phase angle difference cosine values of the driving torque, thus enhancing the electromagnetic torque.

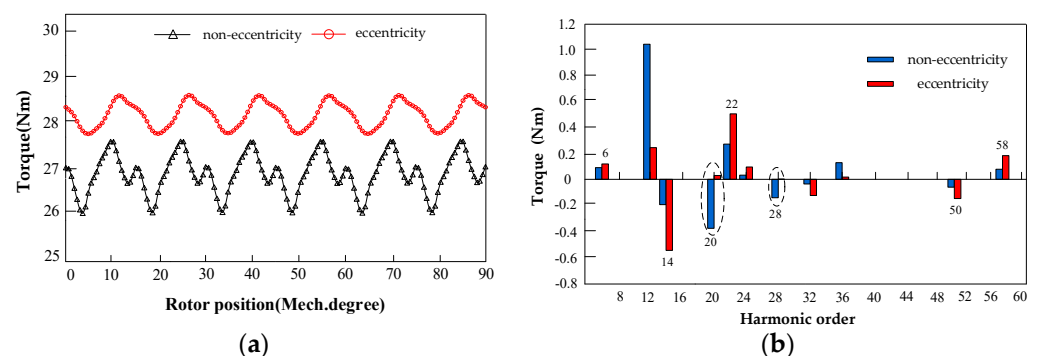


**Figure 11.** The electromagnetic torque generated by air-gap magnetic density harmonics: (a) the torque generated by the fundamental component and (b) the torque generated by the remaining harmonics.

### 3. Optimization of AGE-IPMSM Structural Parameters

The electromagnetic torque of the PMSM is comprises permanent-magnet torque and reluctance torque. According to Equation (16), the permanent-magnet torque is connected

only to the q-axis current and the permanent-magnet flux linkage, while the reluctance torque is affected mainly by the q-axis and d-axis inductance.

$$T_e = \frac{3}{2}p \left[ \psi_f i_q + (L_d - L_q) i_d i_q \right] \quad (16)$$

where  $p$  is the number of pole pairs,  $\psi_f$  is the permanent magnet flux linkage,  $i_d$  and  $i_q$  are the d-axis and q-axis current, respectively, and  $L_d$  and  $L_q$  are the d-axis and q-axis inductance, respectively.

For the sake of improving the output torque, not only to enhance the permanent-magnet torque but also to consider the reluctance torque, it is, therefore, necessary to determine the structural parameters that have a great influence on the optimization objectives, namely the eccentricity distance and the angle between permanent magnets.

### 3.1. Eccentricity Distance Optimization

When selecting the optimal eccentricity distance, it is necessary to determine its variation range. Since the air-gap eccentricity can reduce some magnetic field harmonics, the optimization range of the eccentricity distance is determined by calculating the back-EMF THD. The calculation formula for the back-EMF THD is as follows:

$$THD = \frac{\sqrt{\sum_{h=2}^n U_h^2}}{U_1} \times 100\% \quad (17)$$

where  $U_h$  is the RMS value of the  $h$ th harmonic voltage, and  $U_1$  is the RMS value of fundamental voltage.

The no-load back-EMF waveforms at different eccentricity distance are obtained by the FEA method. Fourier decomposition is performed, and the back-EMF THD at different eccentricity distance are calculated, as shown in Figure 12. The dotted line in Figure 12 represents the upper limit of the back-EMF THD. As the eccentricity distance increases, the THD decreases first and then increases, and the upper limit is 7.07%. Therefore, the variation range of the eccentricity distance is selected to be 0~16 mm, and the eccentricity distance step is 2 mm. When the current angle is  $0^\circ$ , the variation of the electromagnetic torque is as shown in Figure 13a. The electromagnetic torque increases as the eccentricity increases, reaching the maximum value of 28.12 Nm, and the change of eccentricity distance also has a significant influence on the torque fluctuation. The average value of electromagnetic torque and the variation of torque ripple under different eccentricity distance are shown in Figure 13b. It can be seen that the electromagnetic torque gradually tends to be stable and no longer increases when the eccentricity distance  $h$  is greater than 12 mm, while the torque fluctuation gradually cuts down on the augment of eccentricity distance. When the eccentricity  $h = 16$  mm, the torque ripple reaches a minimum value of 1.70%.

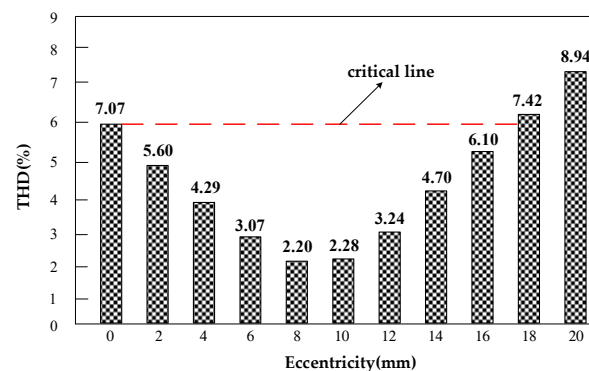
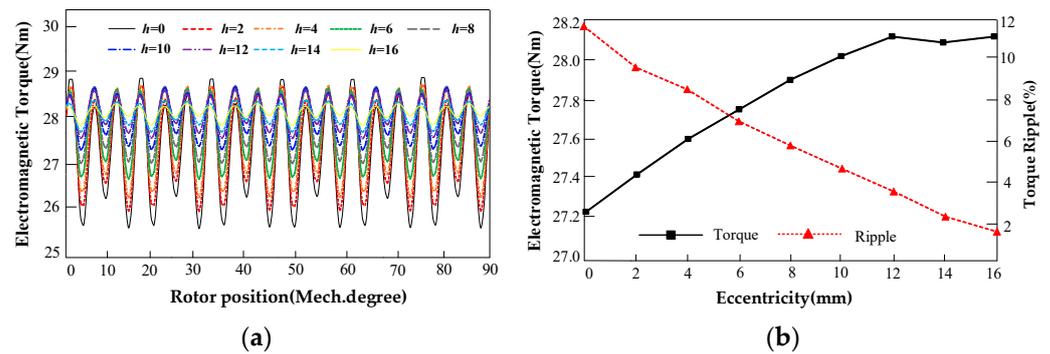


Figure 12. The total harmonic distortion under different eccentricity.



**Figure 13.** (a) Permanent magnet torque under different eccentricity; (b) The average value of permanent magnet torque and torque ripple under different eccentricity.

In conclusion, when the eccentricity distance  $h$  is 12 mm and 16 mm, the electromagnetic torque is 28.12 Nm, and the torque ripple is 3.70% and 1.70%, respectively, but the back-EMF total harmonic distortion from Figure 12 increases by 2.76% when the eccentricity distance  $h = 16$  mm compared with  $h = 12$  mm. Accordingly, the eccentricity distance of 12 mm is chosen as the optimal parameter.

### 3.2. The Angle between the V-Type Permanent Magnets Optimization

In addition to the eccentricity distance, the impact of the angle between permanent magnets on the electromagnetic torque is also studied. The initial angle between permanent magnets is  $96^\circ$ . Due to the limitation of the rotor size, the optimization range is  $108^\circ \sim 84^\circ$ , and the optimization angle step is  $4^\circ$ . When the air gap is eccentric, the current angle of the machine to generate the maximum torque is  $20^\circ$ . Therefore, under the condition of the air-gap eccentricity distance  $h = 12$  mm and the current angle of  $20^\circ$ , the finite element simulation analysis of the seven sets of angles is carried out. The variation of electromagnetic torque under different angles between permanent magnets is shown in Figure 14a. The average electromagnetic torque and torque ripple under different angles between permanent magnets are shown in Figure 14b.

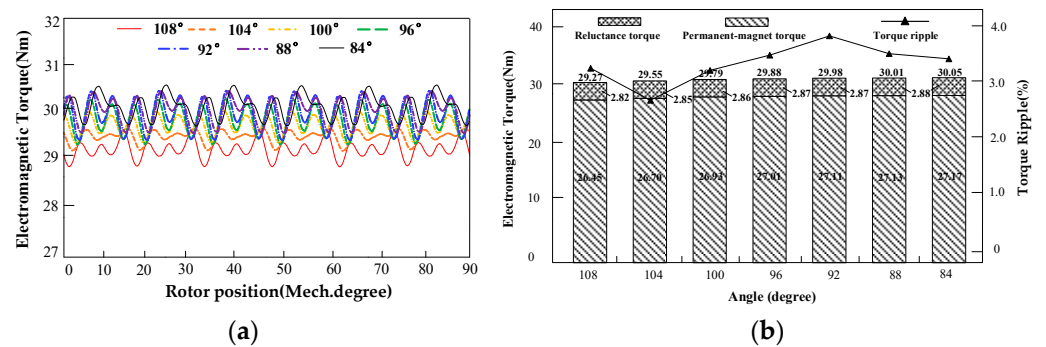


**Figure 14.** (a) Electromagnetic torque with different angle between the V-type permanent magnets; (b) The average value of electromagnetic torque and torque ripple with different angle between the V-type permanent magnets.

The permanent-magnet torque and reluctance torque shown in Figure 14a,b increase with the decrease of the angle between the permanent magnet. When the angle is  $84^\circ$ , the permanent-magnet torque and reluctance torque reach their maxima, which are 27.17 Nm and 2.88 Nm, respectively. Therefore, the maximum electromagnetic torque is 30.05 Nm. Nevertheless, the variation of torque ripple is different from that of electromagnetic torque. When the angle between permanent magnets is  $104^\circ$ , the torque ripple is 1.86%, reaching the minimum.

In addition, the change of the angle between permanent magnets also affects the flux weakening speed range. The machine can reach its ideal maximum speed when both the voltage and current reach their maximum values, and the armature current at this moment is only the d-axis current for demagnetization [24]. The maximum speed can be expressed as:

$$n_{max} = \frac{60u_{lim}}{2\pi p \left| \psi_f - L_d i_{lim} \right|} \quad (18)$$

where maximum voltage  $u_{lim}$ , current  $i_{lim}$ , and pole pair  $p$  are all determined parameters. Therefore, the ideal maximum speed of the machine is related mainly to the permanent magnet flux linkage  $\psi_f$  and the d-axis inductance  $L_d$ . As the angle between the permanent magnets reduces,  $\psi_f$  increases and  $L_d$  decreases. According to Equation (18), it can be obtained that the maximum speed of the machine lowers as the angle between the permanent magnets decreases. The torque–speed characteristics curves of the AGE-IPMSM in the constant-torque and flux weakening range at different angles between the V type permanent magnet are shown in Figure 15, with a maximum speed of 3900 r/min at 108° and 3300 r/min at 84°.

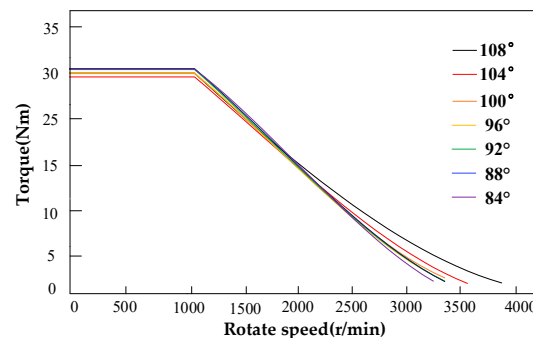


Figure 15. The torque–speed curve with different angle between the V-type permanent magnets.

On the basis of the above comparative analysis of the electromagnetic torque, torque ripple, and maximum speed under different angles between the V type permanent magnets, the optimum angle of 104° was selected. The magnetic flux density plot at rated load is shown in Figure 16a; the flux density of the stator teeth is approximately 1.5 T, which is not saturated, so it has little effect on the transmission of torque. The electromagnetic torque at rated load in the generating condition is shown in Figure 16b, with average torque of 20.41 Nm and torque fluctuation of 4.88%.

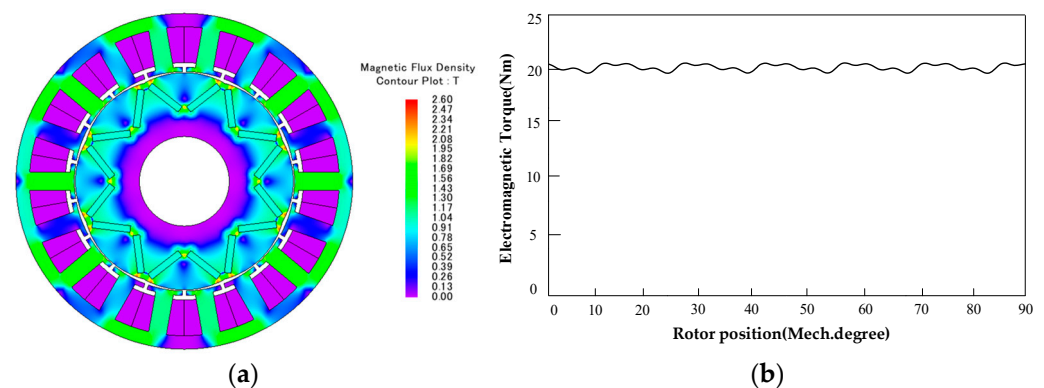


Figure 16. (a) Magnetic flux density plot at rated load (b) Electromagnetic torque at rated load.

Furthermore, the comparison results of torque density and efficiency at rated load are summarized in Table 2. It can be seen that comparing the non-eccentric model with the benchmark machine model, the torque density is reduced by 1.03 kNm·m<sup>-3</sup> after

eccentricity, but the efficiency is increased by 2.5%. Through structural optimization, the phase difference cosine of air-gap flux density harmonics is advanced; thus, the torque density of the post-optimized model is improved. Although the efficiency is reduced to a certain extent, it is still increased by 1.5% compared with the non-eccentric model. Accordingly, the performance of the post-optimized model is better than that of the pre-optimized model.

**Table 2.** Comparison results of torque density and efficiency at rated load.

	Torque (Nm)	Torque Density ( $\text{kNm} \cdot \text{m}^{-3}$ )	Efficiency (%)
Non-eccentricity	22.52	8.50	91.0
Pre-optimality	19.79	7.47	93.5
Post-optimality	20.41	7.70	92.5

#### 4. Prototype Experiment

In accordance with the design parameters in Table 3, an 18-slot/8-pole AGE-IPMSM prototype was manufactured, and an experimental platform was built. The experiment of the prototype for power generation at rated speed was carried out. The experimental platform shown in Figure 17 consists of the prototype, a torque sensor, and a servo motor. The torque sensor measures the torque and speed of the machine, and the servo motor provides the input torque.

**Table 3.** Main performance index and structural parameters of AGE-IPM machine.

Parameters	Value
Rated power/W	2000
Rated current/A	10
Rated speed/(r/min)	1000
Rated frequency/Hz	66.67
Air-gap length/mm	0.5
Stack length/mm	150
Number of pole pairs	4
Material of stator and rotor	50JN470
Stator outside diameter/mm	150
Stator inside diameter/mm	98
Rotor outside diameter/mm	97
Rotor inside diameter/mm	40
Eccentricity distance/mm	12
Number of stator slots	18
Number of phases	3
Number of turns of armature windings	23
Shape of permanent magnet	Rectangle
Length of permanent magnet/mm	150
Width of permanent magnet/mm	17
Thickness of permanent magnet/mm	3

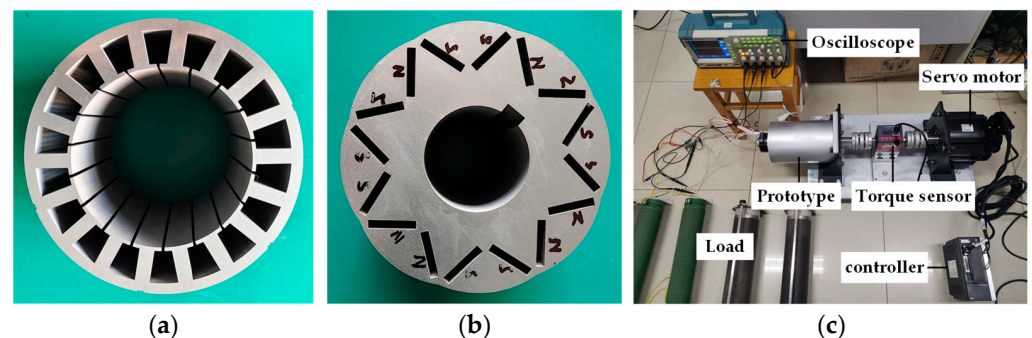


**Figure 17.** Prototype and experimental platform: (a) stator; (b) rotor; and (c) experimental platform.

The no-load back-EMF waveform at the rated speed of 1000 r/min is shown in Figure 18. It can be seen that the RMS value of the measured back-EMF is 107 V, and the FEA calcu-

lated is 108 V. The measured results basically match the FEA results, and the waveform is highly sinusoidal.

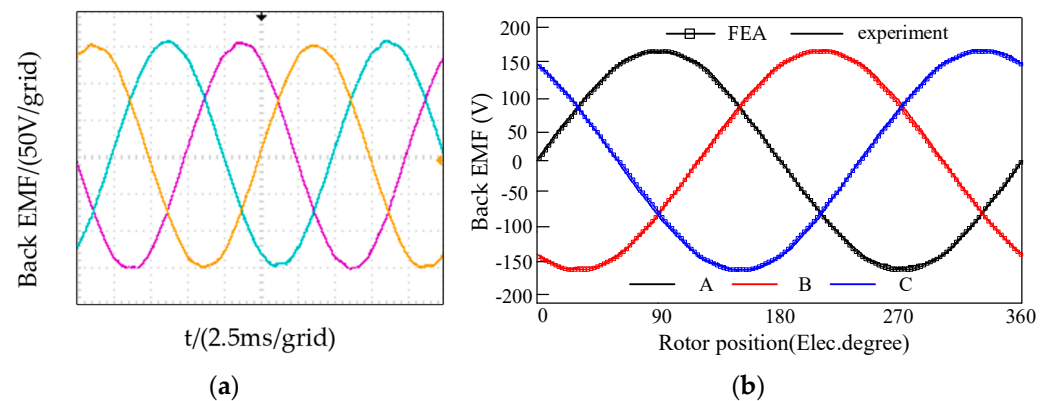


**Figure 18.** Waveforms of back-EMF at no load: (a) measured waveform and (b) comparison of finite element simulation and experimental waveforms of A, B, C three phases of the back-EMF.

For purpose of verifying the torque characteristics of the motor, the load test of the prototype was carried out at a rated speed of 1000 r/min. The FEA calculated and measured electromagnetic torque of the machine at rated speed are shown in Figure 19a. The FEA calculated output torque at rated speed of 1000 r/min is 20.41 Nm, and the measured input torque is 21.41 Nm. Since there are some mechanical losses when the motor runs at no-load, there is a certain error between the measured input torque and output torque, but otherwise the measured result is almost consistent with the FEA calculated value, and the torque fluctuation is also very low, thus verifying the accuracy of the theoretical analysis and FEA results. In addition, the torque–speed curve of the machine is shown in Figure 19b. It can be seen that the maximum speed of the machine reaches 3600 r/min, which is more than three times the base speed, indicating that the machine has better weak magnetic performance.

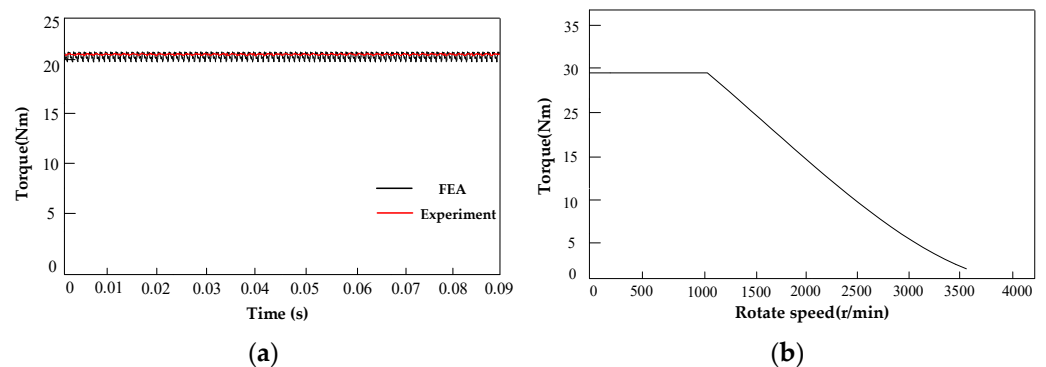


**Figure 19.** (a) Measured and simulated torque; (b) The torque–speed curve of the machine.

## 5. Conclusions

In this paper, the analytic models of no-load and load air-gap magnetic fields with air-gap eccentricity are calculated according to the magnetic circuit analysis theory, and the variations of radial and tangential air-gap magnetic density harmonic amplitude, phase angle difference cosine, and the magnitude of electromagnetic torque before and after air-gap eccentricity are compared and analyzed by Maxwell's tensor method. The results show that the radial and tangential air-gap magnetic density harmonic phase angle difference cosine has a great influence on the electromagnetic torque after air-gap eccentricity. On this basis, the back-EMF total harmonic distortion, electromagnetic torque, and torque ripple are used as optimization targets to optimize the eccentricity distance and the angle between the V-type permanent magnets, and the optimal structural parameters are selected. The

theoretical analysis is verified by the prototype experiments, which show that the air-gap eccentricity reduces the torque fluctuation and advances the output torque by increasing the cosine value of the phase angle difference of the magnetic density harmonics generating the driving torque so that the output characteristics of AGE-IPMSM are improved. Since this paper focuses on the optimization analysis of the machine structure to improve the output characteristics, the control performance of this machine remains to be studied in depth. The adjusting characteristics of the torque or speed control system will be further studied and its dynamic characteristics will be improved next.

**Author Contributions:** Writing—original draft, J.W.; Writing—review & editing, Y.W. All authors have read and agreed to the published version of the manuscript.

**Funding:** This work was supported by the National Natural Science Foundation of China under Grants 52130706.

**Data Availability Statement:** The data is unavailable due to privacy.

**Conflicts of Interest:** The authors declare no conflict of interest.

## References

- Guo, H.; Xu, H.; Xu, J.Q.; Tian, W. Design of an aviation dual-three-phase high-power high-speed permanent magnet assisted synchronous reluctance starter-generator with antishort-circuit ability. *IEEE Trans. Power Electron.* **2022**, *37*, 12619–12635. [[CrossRef](#)]
- Deng, W.; Zuo, S.; Chen, W.; Qian, Z.; Qian, C.; Cao, W. Comparison of eccentricity impact on electromagnetic forces in internal- and external-rotor permanent magnet synchronous motors. *IEEE Trans. Transp. Electr.* **2022**, *8*, 1242–1254. [[CrossRef](#)]
- Liu, F.; Wang, X.; Xing, Z.; Yu, A.; Li, C. Reduction of cogging torque and electromagnetic vibration based on different combination of pole arc coefficient for interior permanent magnet synchronous machine. *CES Trans. Electr. Mach. Syst.* **2021**, *5*, 291–300. [[CrossRef](#)]
- Li, X.L.; Liu, S.W.; Wang, Q.S.; Yan, B.; Huang, Z.N.; Wang, K. Performance investigation and experimental testing of a stator-PM-excitation axial-flux magnetic gear. *IEEE Trans. Transp. Electr.* **2022**. [[CrossRef](#)]
- Li, X.L.; Xue, Z.W.; Yan, X.Y.; Zhang, L.X.; Ma, W.Z.; Hua, W. Low-complexity multivector-based model predictive torque control for PMSM with voltage preselection. *IEEE Trans. Power Electron.* **2021**, *36*, 11726–11738. [[CrossRef](#)]
- Li, X.L.; Xue, Z.W.; Zhang, L.X.; Hua, W. A low-complexity three-vector-based model predictive torque control for SPMSM. *IEEE Trans. Power Electron.* **2021**, *36*, 13002–13012. [[CrossRef](#)]
- Li, X.L.; Lu, K.J.; Zhao, Y.J.; Chen, D.L.; Yi, P.; Hua, W. Incorporating harmonic-analysis-based loss minimization into MPTC for efficiency improvement of FCFMPM motor. *IEEE Trans. Ind. Electron.* **2022**. [[CrossRef](#)]
- Wang, Y.B.; Sun, J.X. Design of interior permanent magnet synchronous machines with fractional-slot concentrated windings. *Trans. China Electrotech. Soc.* **2014**, *29*, 70.
- Pang, D.C.; Shi, Z.J.; Chang, Y.H.; Huang, H.C.; Bui, G.T. Investigation of an Interior micro permanent magnet synchronous motor. *Energies* **2021**, *14*, 4172. [[CrossRef](#)]
- Ding, Z.P.; Bing, Z.; Dejun, Y. A design of fractional-slot concentrated winding IPM synchronous motor for electric vehicles. In Proceedings of the IECON 2017—43rd Annual Conference of the IEEE Industrial Electronics Society, Beijing, China, 29 October–1 November 2017.
- Asef, P.; Perpiñà, R.B.; Laphorn, A.C. Optimal pole number for magnetic noise reduction in variable-speed permanent magnet synchronous machines with fractional-slot concentrated windings. *IEEE Trans. Transp. Electr.* **2019**, *5*, 126–134. [[CrossRef](#)]
- Wang, Y.B.; Wang, Q.S.; Zhu, X.K.; Li, X.L.; Hua, W. An improved critical current calculation method of HTS field-excitation coil for double-stator HTS generator with stationary seal. *IEEE Trans. Energy Convers.* **2022**. [[CrossRef](#)]
- Gao, F.Y.; Qi, X.D.; Li, X.F.; Ta, C.X.; Gao, P. Analytical calculation and optimization analysis of electromagnetic performance of halbach partially-segmented permanent magnet synchronous motors with unequal width and thickness. *Trans. China Electrotech. Soc.* **2022**, *37*, 1404.
- Zhao, W.; Lipo, T.A.; Kwon, B.I. Torque pulsation minimization in spoke-type interior permanent magnet motors with skewing and sinusoidal permanent magnet configurations. *IEEE Trans. Magn.* **2015**, *51*, 2. [[CrossRef](#)]
- Li, F.; Wang, K.; Li, J.; Zhang, H.J. Suppression of even-order harmonics and torque ripple in outer rotor consequent-pole pm machine by multilayer winding. *IEEE Trans. Magn.* **2018**, *54*, 3–4. [[CrossRef](#)]
- Wang, K.; Sun, H.Y.; Zhang, L.F.; Liu, C.; Zhu, Z.Q. An overview of rotor pole optimization techniques for permanent magnet synchronous machines. *Proc. CSEE* **2017**, *37*, 7307.
- Seo, U.; Chun, Y.J.; Choi, P.; Han, D.K.; Lee, J. A technique of torque ripple reduction in interior permanent magnet synchronous motor. *IEEE Trans. Magn.* **2011**, *47*, 3241. [[CrossRef](#)]
- Li, Y.H.; Chai, J.Y.; Mu, S.J.; Sun, X.D. A novel permanent magnet synchronous motor based on armature reaction compensation. *Trans. China Electrotech. Soc.* **2014**, *29*, 27.

19. Liu, G.; Xu, G.; Zhao, W.; Du, X.; Chen, Q. Improvement of torque capability of permanent-magnet motor by using hybrid rotor configuration. *IEEE Trans. Energy Convers.* **2017**, *32*, 956–957. [[CrossRef](#)]
20. Wang, K.; Zhu, Z.Q.; Ren, Y.; Ombach, G. Torque improvement of dual three-phase permanent-magnet machine with third-harmonic current injection. *IEEE Trans. Ind. Electron.* **2015**, *62*, 6836. [[CrossRef](#)]
21. Wang, K.; Zhu, Z.Q.; Ombach, G.; Chlebosz, W. Average torque improvement of interior permanent-magnet machine using third harmonic in rotor shape. *IEEE Trans. Ind. Electron.* **2014**, *61*, 5047–5057. [[CrossRef](#)]
22. Wang, K.; Zhu, Z.Q.; Ombach, G. Torque improvement of five-phase surface-mounted permanent magnet machine using third-order harmonic. *IEEE Trans. Energy Convers.* **2014**, *29*, 735–747. [[CrossRef](#)]
23. Zhu, Z.Q.; Liu, Y. Analysis of air-gap field modulation and magnetic gearing effect in fractional-slot concentrated-winding permanent-magnet synchronous machines. *IEEE Trans. Ind. Electron.* **2018**, *65*, 3691. [[CrossRef](#)]
24. Li, C.Y.; Wang, Y.; Meng, T. Research on flux weakening characteristics of a negative salient pole permanent magnet synchronous motor. *Trans. China Electrotech. Soc.* **2019**, *34*, 476–477.

**Disclaimer/Publisher’s Note:** The statements, opinions and data contained in all publications are solely those of the individual author(s) and contributor(s) and not of MDPI and/or the editor(s). MDPI and/or the editor(s) disclaim responsibility for any injury to people or property resulting from any ideas, methods, instructions or products referred to in the content.